

Numerical Green's Functions for Sub-Faults in 3D: Application to the Newport-Inglewood Fault, Los Angeles Basin

Haijiang Wang*, Heiner Igel*, Alain Cochard*, Michael Ewald*

*Department of Earth and Environmental Sciences, Ludwig-Maximilians-University of
Munich, Theresienstraße 41, D-80333 Munich, Germany*

Version 0.6, Sep 11, 2006.

Deterministic earthquake scenario simulations are playing an increasingly important role in seismic hazard and risk estimation. The numerical calculation of the complete 3D wavefield in the observed frequency band for a seismically active basin remains a computationally expensive task. Our aim is to provide a tool with which we can calculate a large number of different finite-source scenarios for a particular fault or fault system. In order to avoid having to calculate an individual scenario for each kinematic source description we propose the concept of "numerical Green's functions" (NGF): a large seismic fault is divided into sub-faults of appropriate size for which synthetic Green's functions at the surface of the seismically active area are calculated and stored. Consequently, ground motions from arbitrary kinematic sources can be simulated for the whole fault or parts of it by superposition.

To demonstrate the functionalities of the method a strike-slip NGF data base was calculated for a simplified, vertical model of the Newport-Inglewood (NI) fault in the Los Angeles (LA) Basin. As a first example we use the data base to estimate uncertainties of surface ground motion (e.g., peak ground velocity (PGV)) due to hypocentre location for a given final slip distribution. The results show a

complex behavior, with dependence of absolute PGV and its variation on asperity location, directionality and local structure. Hypocentral depth may affect PGV in a positive or negative way depending on the distance from the fault and the location with respect to basin structure.

1. Introduction

The calculation of the complete wave-field for potential large earthquakes in a given seismically active region of known structure will play a central role in reliably estimating shaking hazard (e.g., Olsen and Archuleta, 1996; Olsen, 2000, Ewald *et al.*, 2006). Such calculations will complement hazard estimation based on probabilistic estimates of seismicity (e.g., Gerstenberger *et al.*, 2005) and/or stochastic means to calculate ground motion scenarios based on highly simplified physical models (e.g., Beresnev *et al.*, 1998; Boore, 2003). Earthquake-induced ground motions strongly depend on: (1) the velocity structure and (2) the finite-fault slip histories. The local and regional velocity structure can be estimated and continuously improved using tomographic tools and/or direct measurements (e.g., borehole information). However, the uncertainty concerning rupture processes remains and it is unquestionable that hazard relevant ground motion characteristics for earthquakes of a given size will strongly depend on some rupture properties such as stress drop, source mechanisms, rupture velocity, slip speed, etc.

This poses a formidable problem when faced with the task of estimating ground motion due to one or more “characteristic earthquakes” of a specific seismically active region. In addition to the uncertainties caused by the shallow velocity structure at frequencies relevant to structures, one would have to calculate many different slip scenarios for one presumed earthquake in order to account for rupture related variations. In order to quantify these variations we propose to generate data bases with

Green's functions calculated for discrete models of faults or fault systems for areas with sufficiently well known 3D velocity structure and fault location. The surface ground motions for each sub-fault excitation are stored which allow arbitrary finite fault scenarios to be synthesized at very little computational costs compared to a normal complete 3D calculation, once the database is available. The opportunity to investigate ground motion variations as a function of many different rupture related parameters for a specific area comes at the price of a sufficiently large number of initial 3D simulations for the pre-designed discretized fault and is economical if the number of synthesizations exceeds the number of NGF calculations.

In this paper we introduce the concept of the NGF method, discuss the accuracy of the method as a function of sub-fault size and other earthquake related parameters, and present a first application to a model of the Newport-Inglewood fault in the Los Angeles Basin, namely how the ground motion varies with the hypocentre location while static displacement is unchanged. The method for calculating quasi-dynamic rupture process published in Guatteri *et al.* (2005) is adopted to generate slip history based on randomly pre-created finite slip distributions. This initial study merely aims at discussing the functionalities of this approach with restrictions in terms of lowest model velocities and achievable frequencies and is not "economical" in the sense described above.

Graves and Wald (2001) also calculated a database of Reciprocal Green's Functions by putting the source (double couple point source) at a station and recording the response at the whole 3D grids. Those responses can, reciprocally, be used as Green's Functions to resolve the trade-offs between the source complexity and the 3D elastic media's path effect when doing the finite fault source inversion. Their work focuses on a few stations on the surface where observations about an earthquake are

available, while the fault discretization can reach the same scale of the grid-length adopted by the numerical method.

2. Numerical Green's Functions: Theory and Verification

In the following we introduce the basic concept of the NGF approach and verify it against *known* (i.e., high-resolution) finite fault solutions. A targeted fault plane is divided into uniform, rectangular sub-faults and for each of these sub-faults the corresponding Green's function is calculated using a double-couple source mechanism (here we restrict ourselves to pure strike-slip excitation). Even though in a strict mathematical sense the term *Green's function* is not correct we use it in connection with our source time function (a Delta function in moment rate) and to illustrate the close connection to the concept of *empirical Green's functions* (e.g., Joyner and Boore, 1986; Hutchings and Wu, 1990; Bour and Cara, 1997; Kohrs-Sansorny *et al.*, 2005). The calculations can be carried out using any numerical solution to the 3D wave propagation problem. Here we employ a high-order staggered-grid finite-difference approach (e.g., Igel *et al.*, 1995; Gottschämmer and Olsen, 2001) with efficient absorbing boundaries based on the concept of perfectly matched layers (e.g., Collino and Tsogka, 2001; Marcinkovich and Olsen, 2003).

Theory and verification

What affects seismic motion can be subdivided into two aspects: the subsurface structure and the seismic source including the focal mechanisms and the slip histories. For one small seismic source i (small enough to be considered as a point source within a certain frequency range), the j -th component of the ground velocity v_j at the location \mathbf{x} and time t , can be expressed as:

$$v_j(\mathbf{x}, t) = g_{ij}(\mathbf{x}, t + \tau_i) * s_i(\tau_i) \cdot \mu_i \cdot A_i, \quad (1)$$

where * indicates time convolution. The term $g_{ij}(\mathbf{x}, t)$ gives the j -th component of ground velocity recorded at location \mathbf{x} at time t and excited by a unit source (in our case a strike slip). $s_i(\tau_i)$ is the source slip rate with fault-area A_i . τ_i is time relative to the origin time of the i -th sub-fault, μ_i is the shear modulus. The resulting scalar seismic moment, M_{0i} , is calculated as $\int s_i(\tau_i) \cdot \mu_i \cdot A_i \cdot d\tau_i$ which is used to scale the $s_i(\tau_i)$ to the correct amplitude.

When an earthquake occurs, each part of its fault plane is excited after a time delay τ_i^0 representing the rupture front arrival time. If all the N NGFs of the fault plane are available, we can employ the following basic equation to sum all the NGFs convolved with the corresponding source functions to calculate the ground velocity for the finite source rupture (which is similar to the numerical solution of the representation theorem given in Bour and Cara, 1997):

$$v_j(\mathbf{x}, t) = \sum_{i=1}^N g_{ij}(\mathbf{x}, t + \tau_i - \tau_i^0) * s_i(\tau_i) \cdot \mu_i \cdot A_i, \quad (2)$$

where $v_j(\mathbf{x}, t)$ is the j -th component of ground velocity at time t for a receiver located at position \mathbf{x} . The linear summation is carried out over all N sub-faults occupied by the target earthquake fault plane. All the sub-fault slip rate functions are scaled correctly to sum up to the total moment M_{tot} of the finite-source earthquake, $M_{tot} = \sum_{i=1}^N \mu_i D_i A_i$, where D_i is the final slip of the i -th sub-fault, i.e., the integration of $s_i(\tau_i)$ over its rise time. Hutchings (1991, 1994) theoretically obtained the same equation from the representation theorem presented by Aki and Richards (2002).

Verification - homogeneous model

Considering that the goal of the NGF method is to be able to synthesize - within some limits (e.g., reliable frequency range) - complete ground motions from arbitrary finite source scenarios on a discretized fault, and that the generation of an NGF data base is computationally expensive, one should attempt to find a minimum number of sub-faults necessary to determine the ground motion with sufficient accuracy. The *optimal* (largest) size of such sub-faults is expected to depend on (1) earthquake fault dimension, (2) the desired frequency band for the synthesized ground motions (i.e., the shortest wavelengths to be described in the 3D velocity model), (3) the properties of the ruptures themselves (magnitude, rupture speed, slip velocity, rise time etc.) and (4) the angle of the receiver relative to the rupture propagation (directivity). This dependency was thoroughly investigated for a homogeneous medium (with parameters shown in table 1). At first, seismic motions from a set of double-couple point sources at different depths, 1 km from each other are calculated and stored (Fig. 1 solid circles). The seismograms recorded at the surface can be used as Green's functions. With appropriate horizontal space shifting, Green's functions corresponding to a planar vertical fault (Fig. 1, hollow circles) can be acquired and finally synthesized to calculate the ground motions for a large earthquake (with appropriate kinematic rupture processes are pre-chosen). The parameters for those kinematic rupture processes are defined in the following way. The fault dimensions of an Mw 7 earthquake and an Mw 6 earthquake are first chosen as 40×20 km and 13×9 km, respectively, and posed such that the strike direction is parallel to the x-axis of the study area. The top of the fault plane is set to be 1 km from the free surface (Fig. 1) and the hypocentre is fixed at the point with smallest x value and depth (Fig. 1, big asterisk). The rupture propagates circularly from the hypocentre to the other parts of fault plane with a constant velocity. The scalar moment M_0 is related to the moment magnitude Mw as $\log M_0 = 1.5M_w + 16.05$ (Kanamori, 1977). The final average slip D is calculated as

$D=M_0/(\mu A)$ and a uniform static slip distribution is used. The slip-rate function for each sub-fault in the time domain is assumed to be a ramp function whose rise time is calculated as the ratio between the local static slip and the presumed constant slip velocity (Table 1).

The solution with sub-fault size of 0.5×0.5 km is first calculated and used as the “*continuous*” solution (Hutchings and Wu, 1990). The misfit energy (ME) between the seismograms from the differently discretized solutions (Fig. 2a, top left corner, two seismograms from different solutions are shown as an example), like sub-faults with side-length of 2.0 km, 3.0 km and 4.0 km, respectively, and the “*continuous*” solution is used to directly measure the accuracies corresponding to the discretized solutions:

$$ME = \frac{\sum_{i=1}^{nt} (v_c(i\Delta t) - v_d(i\Delta t))^2}{\sum_{i=1}^{nt} (v_c(i\Delta t))^2} \times 100 \quad (3)$$

where $v_c(i\Delta t)$ is the “*continuous*” solution’s velocity and $v_d(i\Delta t)$ is the discretized solution’s velocity at time $i\Delta t$, respectively.

First, in Fig. 2a, the ME distribution on the surface between the solution of 4.0 km and the “*continuous*” solution is shown to exhibit the directivity effect on the accuracy for an Mw 7 earthquake. In the triangle area right behind the rupture propagation, the ME values are largest with maximum values of 12% right on the line opposite to the rupture direction. Secondly, three Mw 6 earthquakes with different sub-fault sizes are simulated. The resulting seismic motions are low-pass filtered (Gaussian) with different cut-off periods to investigate the cut-off frequency effect on the accuracy. The resulting largest ME values (of the whole study area) are shown in Fig. 2b as a function of the cut-off period. When the seismograms are filtered with cut-off period of 4.0 s, the maximum ME values of the study area, for all three differently

discretized solutions, respectively, are smaller than those filtered with cut-off period of 3.0 s. Thirdly, nine Mw 6 earthquakes (three different rupture velocities times three different sub-fault sizes) are calculated and the resulting largest ME values of the study area are shown in Fig. 2c as function of rupture velocity, from which we concluded that the accuracy increases with the rupture velocity. Finally, with the other mentioned three parameters kept constant, the magnitude (fault dimension) increase will lead to lower ME of the discretized solution as can be seen in Fig. 2d.

3. Study area and NGF data base

We apply the NGF method to the Newport Inglewood (NI) fault system located in the Los Angeles basin (Fig. 3). An area of 110×100×30 km, in the two horizontal and vertical directions, is selected as study area, and rotated in order to have one horizontal grid axis parallel to the NI fault. The velocity model is based on the elastic part of the SCEC 3D velocity model for the Los Angeles (LA) basin (Version 3, Kohler *et al.*, 2003). The depth of a shear wave velocity isosurface, 2.0 km/s, is shown in Fig. 4. The NI fault is chosen for several reasons: it hosted the M6.4 Long Beach earthquake in 1933 (Hauksson and Gross, 1991), causing serious damage; it is still considered the most probable source for a damaging earthquake to the LA area; the near-vertical plane can be approximated by a vertical plane to first order in the numerical calculation and the predominant right-lateral slip can be approximated with a pure strike-slip mechanism (Grant and Shearer, 2004). The main goal of the current study is to demonstrate the NGF concept and its functionalities. To reduce the computational effort and the size of the data base we truncate the seismic velocities at 1.4 km/s.

The accuracy of the synthesized ground motions as a function of sub-fault size is investigated for an Mw 7 earthquake with the computational setup and source

parameters given in Table 2 (what should be pointed out is that the grid distance is decreased to 0.3 km to fulfill the requirement by the finite difference method). The fault length L and width W are chosen to be 36 km and 18 km, respectively, with the aim that the final fault geometry will be 120×60 (in grid points), which can be divided into sub-faults with size of 3×3 , 4×4 , 5×5 and 6×6 (in grid points). An Mw 7 finite fault earthquake scenario (quasi-dynamic rupture process calculated with the method of Guatteri *et al.*, 2005, 2D Gaussian auto-correlation function with an isotropic correlation-length of 5 km is adopted, and the final slip distribution is shown in Fig. 3, top right corner) is simulated with three different equilateral sub-faults of side-length 0.3 km (treated as the “*continuous*” solution, corresponding to the finest grid distance), 1.5 km, and 1.8 km. The ground motions for the latter two sub-fault sizes are compared to those for the “*continuous*” solution.

As an indicator of the accuracy we compare the peak ground velocity (PGV) over the whole study area covering frequencies up to 0.5 Hz. This choice is somewhat arbitrary and other wave-field characteristics could be used (e.g., shaking duration, or a misfit criterion w.r.t. the “*continuous*” solution). Our specific goal here is to demonstrate that hazard-relevant variations due to finite-source scenarios can be efficiently carried out using the NGF methodology.

PGV difference (x-component) between one discretized solution (sub-fault size of 1.8 km) and the “*continuous*” solution is shown in Fig. 5a (note the sign of the PGV difference). The largest difference is -0.056 m/s (note the minus) in the position of the largest PGV (1.1 m/s). The ratio between the largest PGV difference and the corresponding “*continuous*” velocity amplitude is 5.09%. The waveforms from different solutions are almost identical in the profile shown in Fig. 5c with lowest peak correlation coefficient value of 0.991. This can also be seen from the waveform comparison (Fig. 5b) for one single station where the biggest PGV difference is observed (point P1, Fig.

5a). The maximum amplitude difference between the solution for 1.5 km sub-fault side-length and the “*continuous*” one is 0.035 m/s while that for the solution for 1.8 km is 0.056 m/s. Thus we conclude that solution for 1.5 km sub-fault side-length is accurate enough and can be applied to the generation of the NGF data base. The conclusion about the trend of the accuracy as a function of cut-off frequency (as shown for the homogeneous case) still holds in the 3D heterogeneous case. These results justify the choice of the final parameter setup used to calculate a complete set of NGFs for M7 earthquakes on the NI fault estimated to cover an area of 69x20 km² (Jennings, 1994). As we primarily focus on differential effects we calculate 13 (along depth) x 40 (along strike) sub-fault NGFs (side length 1.5km) for a grid spacing of 300 m and seismograms up to 0.5 Hz. The complete NGF data base for the 140x166 equally spaced surface grid at 600 m distance, for 6 motion components (three translations and three rotations), for all sub-faults at a sampling rate of 100 Hz (decided by the temporal step of FD method), requires approximately 1.5 TByte storage space.

4. Source-related inter-event variations of 3D ground motions: effect of hypocentre location

The NGF data base thus calculated allows us - within the limits of the method (e.g., reliable frequency range) - to synthesize ground motions from arbitrary strike-slip histories on the NI fault for the complete study area. A question of considerable practical relevance to estimates of seismic hazard is how variations of the hypocentre location for a given final slip distribution influence the shaking for a *characteristic* earthquake of a given magnitude. Amongst many other possibilities, this is the question we will focus on in this sample study: we assume the existence of a *characteristic* M7 earthquake on the entire NI fault and synthesize ground motions for a 4x6 regular grid of hypocentre locations in the seismogenic zone (5 - 15 km depth) as indicated in Fig. 3

(inlet). The final slip distribution is generated randomly with a given isotropic correlation length (5 km) based on 2D Gaussian auto-correlation space function (equation 1, Guatteri *et al.*, 2005). The slip histories are calculated quasi-dynamically following Guatteri *et al.* (2005) accounting for the accelerating tendency of the crack front due to dynamic loading and the high stress-drop promotion of fast rupture propagation. The shear-modulus on the fault is kept constant and corresponds to a shear velocity of 3.2 km/s.

In Fig. 6, snapshots of the y-component velocity on the surface are shown. Source and basin related effects on ground motion are distinct in this figure. Most energy is recorded at the area left to the fault plane due to the unilateral rupture propagation from right to left. Wave propagation is slowed down by the basin with low velocity in the area A1 and A2. In the area B where the deepest parts of the study area is, trapped energy and reverberation is observed at time 43 s and also basin amplification on the wave fronts are apparent which can also be seen, more clearly, in one velocity profile shown in Fig. 5c.

Two examples of the resulting PGVs in the LA basin are shown in Fig. 7a, 7b for the hypocentre locations H1 (5km depth, located at SE fault edge) and H2 (15 km depth, located towards the centre) as indicated in Fig. 3 (inlet). The shallow hypocentre with unilateral rupture propagation (H1, Fig. 7a) leads to a directivity-dominated distribution of PGVs towards the NW end of the fault, while the PGVs of the bilaterally propagating rupture from the deeper hypocentre (H2, Fig. 7b) show a clear distance dependence from the fault with dominant PGVs in the NW part. This is due to the main slip occurring in the northern part of the fault (see Fig. 3, inlet). However, it is important to note that the deeper hypocentre illuminates the entire basin leading to considerable more basin-wide shaking compared to the shallower hypocentre.

The parameter study in the hypocentre space allows us to extract the PGVs of all 24 simulations (Fig. 7c) containing the dominant features of the previously shown two examples with basin wide shaking, fault-distance dependent ground motion, and peak motions above the fault area with the largest slip (asperity). The variations of the hypocentre-dependent ground motions can be expressed by relating the variance of the PGV to the mean PGV at each point of the surface grid (Fig. 7d). The resulting distribution illustrates the regions in which most variations of ground motions are to be expected from the hypocentre location. These variations are surprisingly symmetric around the fault edges with some amplification from the basin edges particularly on the SE end. It is interesting to note that - except at the fault edges - the variations are considerably larger inside the basin but at some distance from the fault.

We complete this study by investigating the relationship between PGV and source depth for all simulated scenarios and two receivers indicated in Fig. 8 (R1, 40 km from the fault, inside the basin; R2, above the centre of the fault). Considering the energy geometry spreading or attenuating, more effects due to 3D structure are expected for ground motions recorded at R1 (far from the fault) and more effects due to source process are expected for R2 (close to the fault). Horizontal velocity seismograms (fault-parallel component) are shown for receivers R1, R2 and four different hypocentral depths (same epicentre) as indicated in Fig. 3 (inlet, white rectangle). The PGVs (and variance) for all 24 simulations at receivers R1, R2 are displayed as a function of source depth in Fig. 8c, 8d, respectively. For the distant receiver (R1, Fig. 8c) the mean PGV increases slightly with source depth, while the variance is much larger for deeper events, indicating a stronger path-dependence for wave fields arriving from deep sources than from shallow sources. The opposite behaviour is observed for receiver R2 close to the fault (Fig. 8d). The mean PGV and its variance decrease with source depth indicating that the upward propagating rupture and the associated directivity effect dominates the PGV in this region.

5. Conclusions

We introduced the concept of numerical Green's functions (NGF) that can be applied to discretized faults or fault systems in 3D media allowing the calculation of earthquake scenarios from arbitrary slip histories. NGF data bases allow a systematic study of source related uncertainties/variations of seismic hazard relevant wave field properties (peak ground motions, static displacements and rotations, shaking duration, etc.) varying slip distributions (e.g., asperity locations), slip and rupture velocities, hypocentre locations, etc. Particularly interesting is the possibility to apply high-resolution slip histories from dynamic rupture simulations and investigate their relevance to shaking hazard.

Our simple example on the influence of hypocentre location on the resulting ground motions indicates complex behaviour with dependence of absolute PGV and its variation on asperity location, directionality and local structure. In addition, hypocentral depth may affect PGV in a positive or negative way, depending on the distance from the fault, and location with respect to basin structure.

This study was subject to severe limitations. Amongst others, (1) the fault is approximated by a vertical plane and strike-slip source mechanism. (2) The lowest shear-velocity (1.4 km/s) is too high to be useful for realistic hazard estimates and the highest frequencies are only relevant for very tall buildings. (3) We limited ourselves to investigate only one M7 earthquake happening on the same fault with the same final slip distribution. Yet, the main purpose of this study is to illustrate the potential functionalities of an NGF data base and the possibilities to systematically investigate source related uncertainties in 3D areas with high seismic hazard. Source related uncertainty in 3D media is an issue that has so far not been addressed properly, partly due to limitations of computational resources. It is important to note that such NGF data bases only make sense if the crustal structure is sufficiently well known and that the

NGFs would need to be recalculated with every model update (it might be possible to devise approximate updates of the NGFs). Nevertheless, we suggest that this methodology may be useful also on a larger scale particularly for mega-faults in subduction zones with tsunami-generating potential.

Acknowledgements

This work was partially funded by the International Quality Network - Georisk (German Academic Exchange Service), and the Elite Graduate College THESIS (elite.geophysik.uni-muenchen.de). We also acknowledge support from the European Human Resources Mobility Programme (Research Training Network SPICE, www.spice-rtn.org) and the provision of computational resources through the Leibniz Computing Centre Munich. ME was partly funded by the KONWIHR project and a stipend of the MunichRe.

References

- Aki, K., and P. G. Richards (2002), *Quantitative seismology*, 2nd Edition, University Science Books.
- Beresnev, I. A., G. M. Atkinson, P. A. Johnson, and E. H. Field (1998), Stochastic finite-fault modelling of ground motions from the 1994 Northridge, California, earthquake. II. Widespread nonlinear response at soil sites, *Bull. Seism. Soc. Am.*, **88**, 1402-1410.
- Boore, D. M. (2003), Simulation of ground motion using the stochastic method, *Pure and Applied Geophysics*, **160**, 635-676.

- Bour, M., and M. Cara (1997), Test of simple empirical green's functions method on moderate-sized earthquakes, *Bull. Seism. Soc. Am.*, **87**, 668-683.
- Collino, F., and C. Tsogka (2001), Application of the PML absorbing layer model to the linear elastodynamic problem in anisotropic heterogeneous media, *Geophysics*, **66**, 294-307.
- Ewald, M., H. Igel, K. G. Hinzen, and F. Scherbaum (2006), Basin-related effects on ground motion for earthquake scenarios in the Lower Rhine Embayment, *Geophys. J. Int.*, in print.
- Gerstenberger, M. C., S. Wiemer, L. M. Jones, and P. A. Reasenber (2005), Real-time forecasts of tomorrow's earthquakes in California, *Nature*, **435**, 328-331.
- Gottschämmer, E., and K. B. Olsen (2001), Accuracy of explicit planar free-surface boundary condition implemented in a fourth-order staggered-grid velocity-stress finite-difference scheme, *Bull. Seism. Soc. Am.*, **91**, 617-623.
- Grant, L. B., and P. M. Shearer (2004), Activity of the offshore Newport - Inglewood Rose Canyon fault zone, coastal Southern California, from relocated microseismicity, *Bull. Seism. Soc. Am.*, **94**, 747-752.
- Graves, R. W., and D. J. Wald (2001), Resolution analysis of finite fault source inversion using one- and three-dimensional Green's functions 1. Strong motions, *J. Geophys. Res.*, **106**, 8745-8766
- Guatteri, M., P. M. Mai, and G. C. Beroza (2005), A pseudo-dynamic approximation to dynamic rupture models for strong ground motion prediction, *Bull. Seism. Soc. Am.*, **94**, 2051-2063.
- Hauksson, E., and S. Gross (1991), Source parameters of the 1933 Long Beach earthquake, *Bull. Seism. Soc. Am.*, **81**, 81-98.
- Hutchings, L., and F. Wu (1990), Empirical Green's functions from small earthquakes - a waveform study of locally recorded aftershocks of the San Fernando earthquake, *J. Geophys. Res.*, **95**, 1187-1214.

- Hutchings, L. (1991), "Prediction" of strong ground motion for the 1989 Loma Prieta earthquake using Empirical Green's Functions, *Bull. Seism. Soc. Am.*, **81**, 1813-1837.
- Hutchings, L. (1994), Kinematic earthquake models and synthesized ground motion using Empirical Green's Functions, *Bull. Seism. Soc. Am.*, **84**, 1028-1050.
- Igel, H., P. Mora and B. Riollet (1995), Anisotropic wave propagation through finite-difference grids, *Geophysics*, **60**, 1203-1216.
- Jennings, C. W. (1994), Fault activity map of California and adjacent Areas with location and ages of recent volcanic eruptions. *California Geologic Data Map Series*, Map No. **6**. California Division of Mines and Geology.
- Joyner, W. B. and D. M. Boore (1986), On simulating large earthquakes by Green's-function addition of smaller earthquakes. *Earthquake Source Mechanics*, Geophysical Monograph No. 37 (Maurice Ewing, ed.), **8**, 269-274.
- Kanamori, H. (1977), The energy release in great earthquakes, *J. Geophys. Res.*, **82**, 2981-2987.
- Kohler, M., H. Magistrale, and R. Clayton (2003), Mantle heterogeneities and the SCEC three-dimensional seismic velocity model version 3, *Bull. Seism. Soc. Am.*, **93**, 757-774.
- Kohrs-Sansornny, C., F. Courboux, M. Bour, and A. Deschamps (2005), A Two-stage method for ground-motion simulation using stochastic summation of small earthquakes, *Bull. Seism. Soc. Am.*, **95**, 1387-1400.
- Marcinkovich, C., and K. B. Olsen (2003), On the implementation of Perfectly Matched Layers in a 3D fourth-order velocity-stress finite-difference scheme, *J. Geophys. Res.*, **108**, 2276-2293.
- Olsen, K. B. (2000), Site amplification in the Los Angeles basin from 3D modelling of ground motion, *Bull. Seism. Soc. Am.*, **90**, S77-S94.

Olsen, K. B. and R. J. Archuleta (1996), 3D-simulation of earthquakes in the Los Angeles fault system, *Bull. Seism. Soc. Am.*, **86**, 575-596.

Table 1: Verification setup for the homogeneous case

Spatial discretization (m)	1000
Temporal discretization (s)	0.0822
S-wave velocity (km/s)	3.9
Simulation time (s)	50
Study area (km)	150x130x60
PML Nodes	10
Constant slip rate (m/s)	1

Table 2: Verification setup for the heterogeneous model in the Los Angeles basin

Spatial discretization (km)	0.300
Temporal discretization (s)	0.01811
Lowest S-wave velocity (km/s)	1.400
Simulation time (s)	65
Number of cells	550x500x150
PML Nodes	10
Fault area (km ²)	18x36

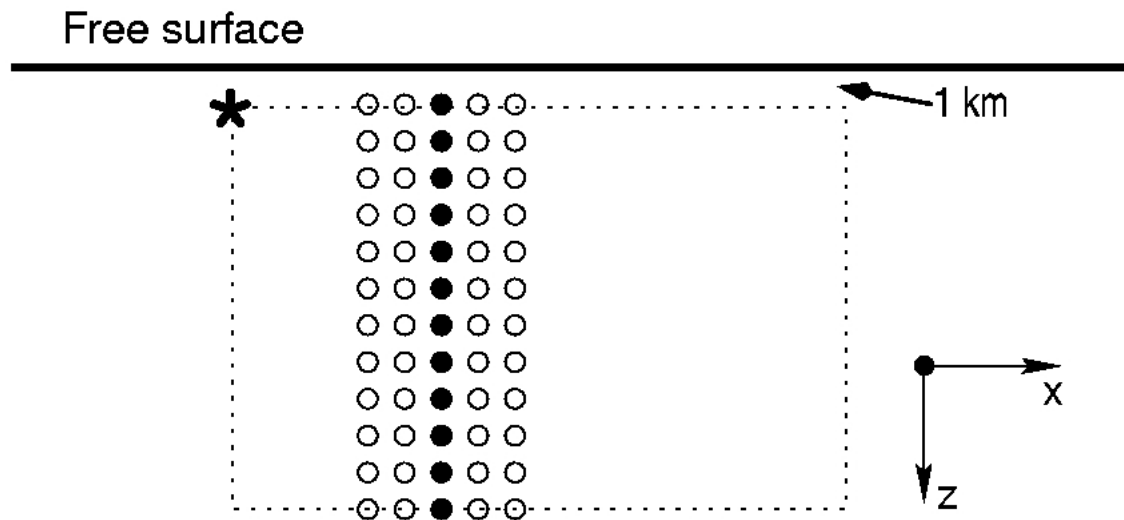


Figure 1: Schematic set-up for the homogeneous case. The thick black line is the free surface. Black solid circles are the hypocentres of a set of double-couple point sources and the big asterisk marks the fixed hypocentre location (left top corner) for an earthquake whose fault plane is represented by the thin dashed rectangular (which is uniformly discretized and represented with cycles, solid and open).

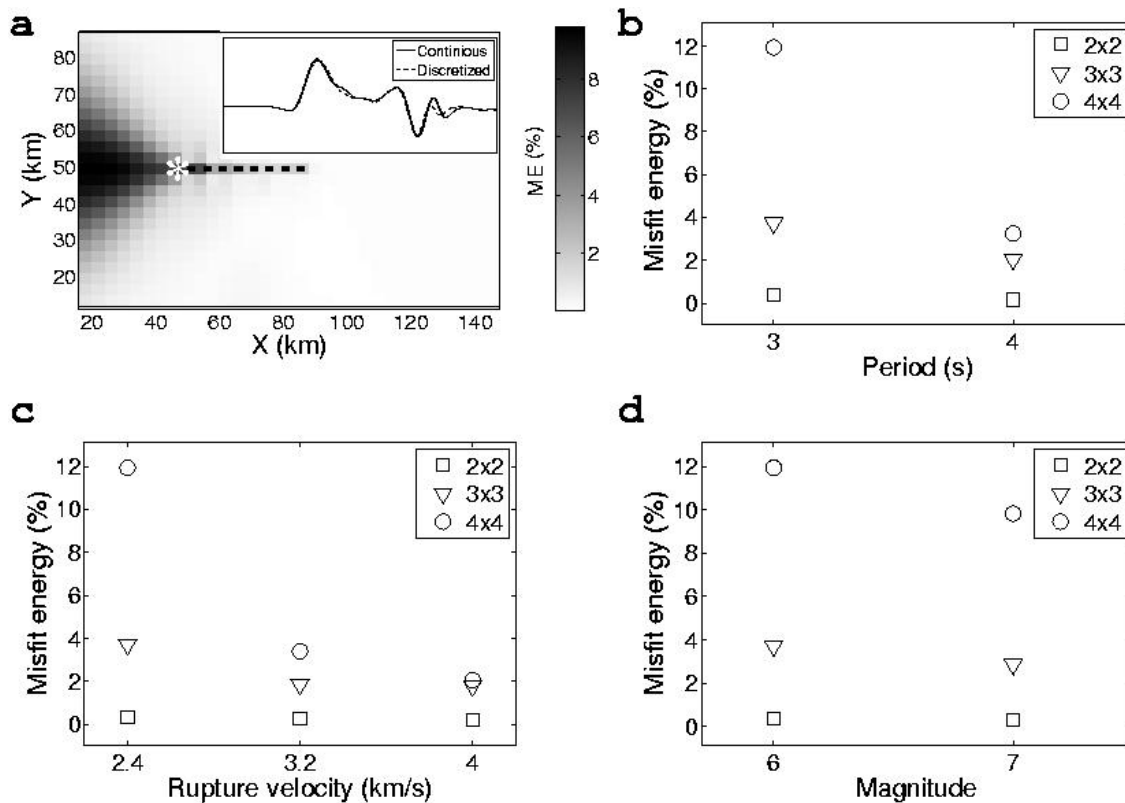


Figure 2: Accuracy of seismogram synthesis as a function of sub-fault size, frequency range, rupture velocity and magnitude. **a.** Misfit energy (ME) (%) (see equation (3)) at each surface grid between sub-fault size 4x4 km and “continuous” solution (0.5x0.5 km). In the inset two velocity seismograms are shown. Thick dashed line (40 km in length) marks the Mw 7 fault trace on the surface in which that of Mw 6 (13 km in length) starts from the left tip. White asterisk marks the epicentres with the assumption of unilateral rupture propagation. **b.** ME as a function of cut-off period (Gaussian low-pass filtering). **c.** ME as a function of rupture velocity. **d.** ME as a function of magnitude. x-component of velocity is used in this figure for the reason that it is the least accurate.

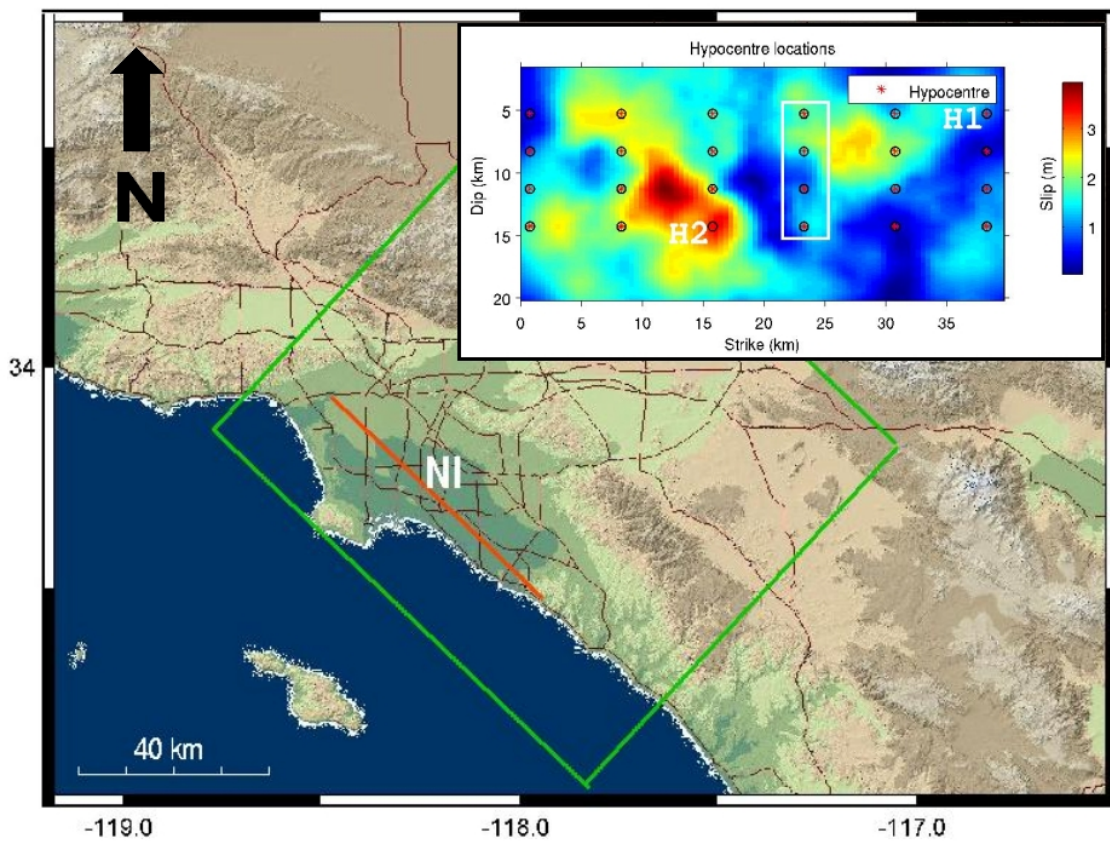


Figure 3: Los Angeles area with modelled region (green rectangle) and the idealized Newport-Inglewood fault (NI, red line). Inlet: Final horizontal slip distribution of an M7 earthquake on the vertical NI fault plane and hypocentre grid (red asterisks, for investigation of hypocentral effect on ground motion). H1 and H2 show the two example hypocentre locations for more detailed exhibition of hypocentral effect on ground motion.

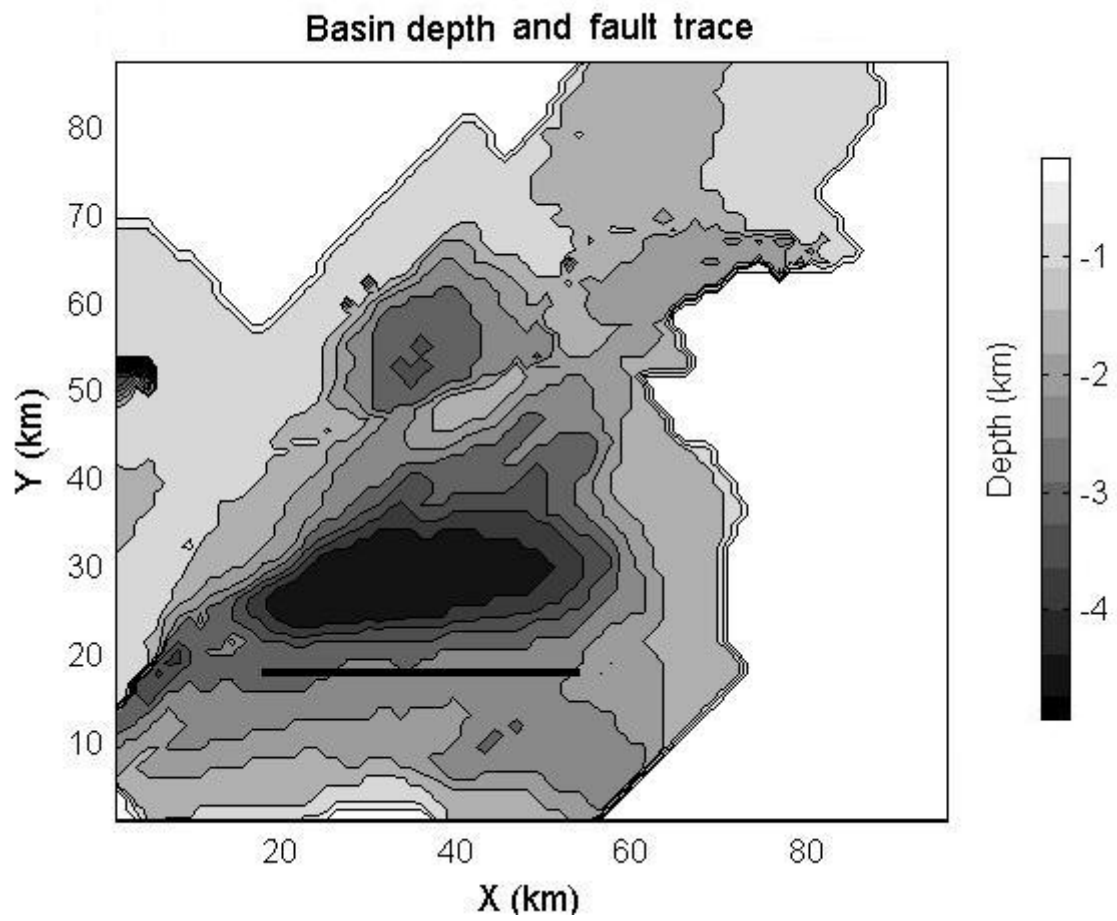


Figure 4: Depth of shear wave velocity isosurface at value of 2.0 km/s (grey scale). The thick black line marks the fault trace of the M7 earthquake.

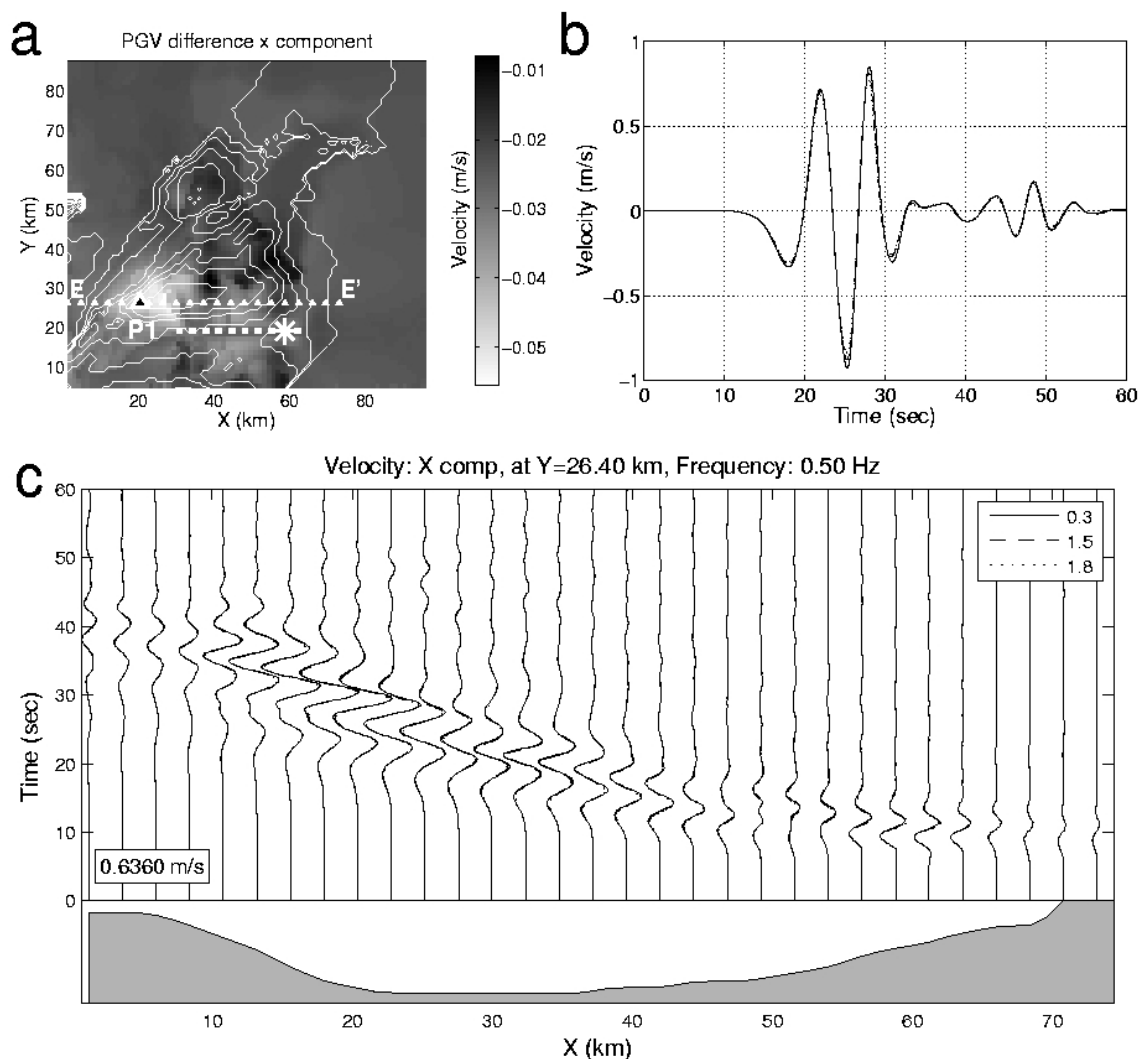


Figure 5: Optimal sub-fault size determination for an M7 earthquake in LA basin. **a.** PGV difference distribution between the discretized solution of 1.8 km and the “continuous” solution where dashed thick white line marks the fault trace and the big asterisk, the epicentre. The biggest PGV difference is observed at station P1. **b.** Velocity seismograms of differently discretized solutions, i.e. 0.3 km, 1.5 km and 1.8 km, respectively, for station P1 in a. **c.** Velocity profile, EE’ (a), of differently discretized solutions. The grey area at the bottom shows the isosurface depth of shear wave velocity at value of 2 km/s.

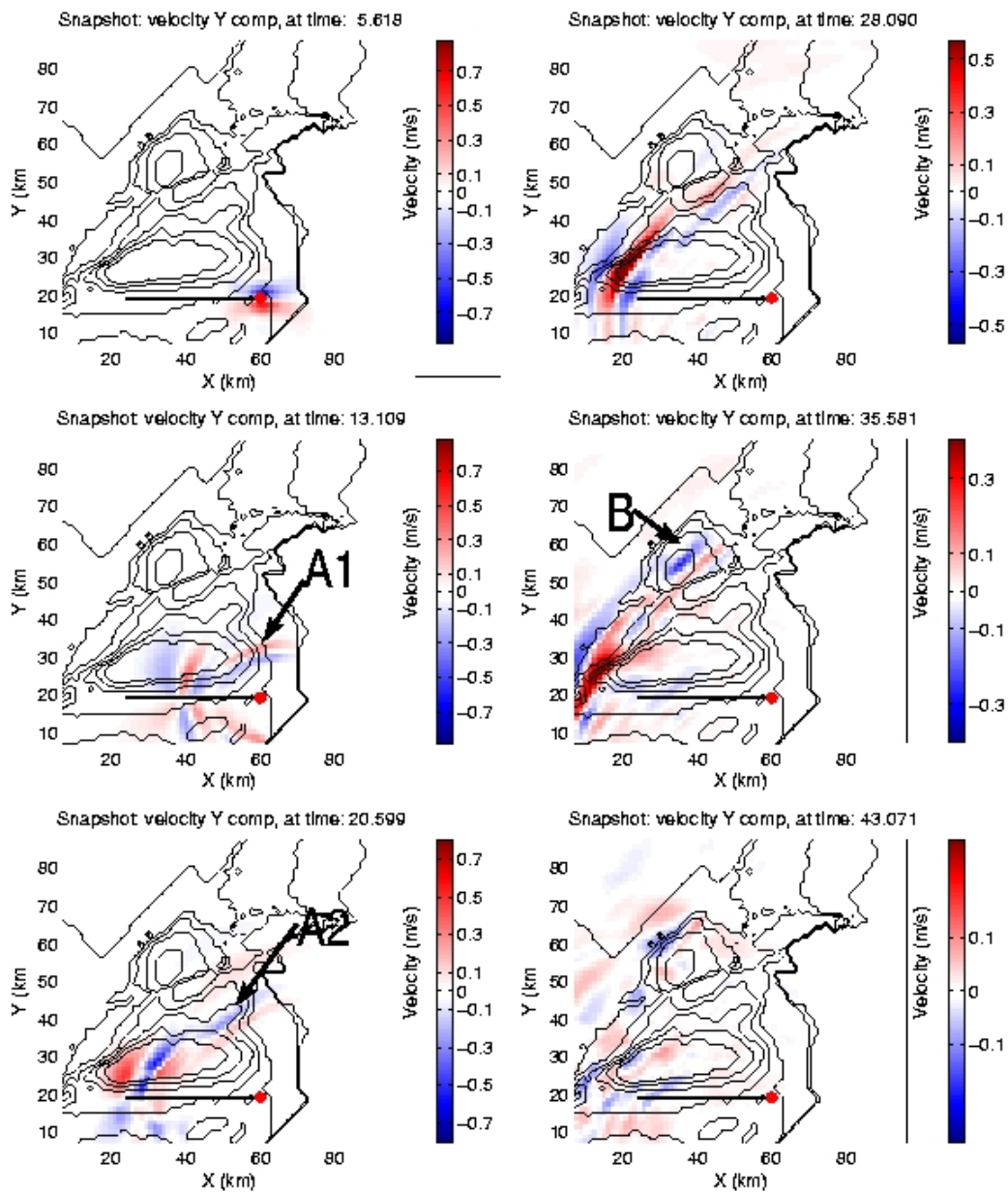


Figure 6: Velocity snapshots of y-component at different times (according to hypocentre H1, Fig. 3, inlet). Black thin lines show the contours of isosurface of shear wave velocity at value 2 km/s. Thick black line shows the fault trace on which red asterisk marks the epicentre. Note the change of the color scale. Areas A1, A2 and B are depicted out to illustrate the structure effect on wave propagation.

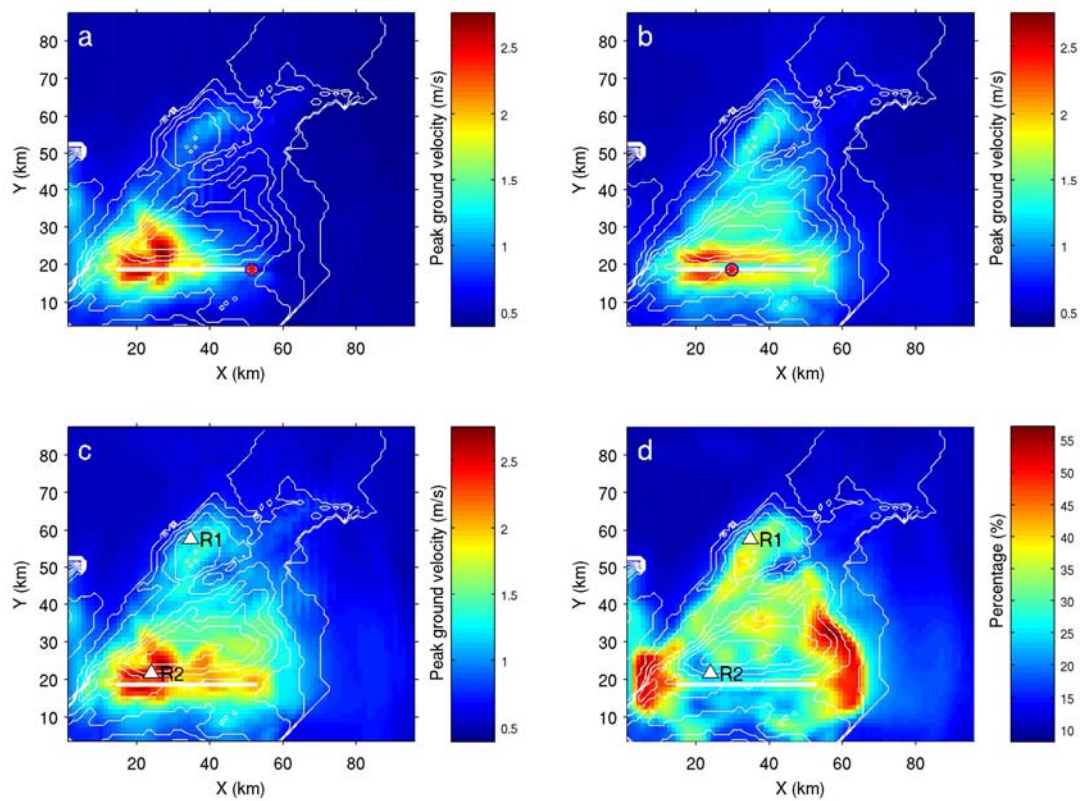


Figure 7: **a.** Peak ground velocity (PGV, modulus of horizontal components) for hypocentre H1. **b.** Same for H2. The epicentres are indicated as red asterisks. The straight white line indicates the fault trace. Thin white lines are contours of the seismic velocity model. **c.** Maximum of PGVs for the combination of all 24 simulations. **d.** The ratio between the standard deviation and the mean PGV value (combination of all 24 simulations, too) in percent. R1 and R2 are the two example positions chosen to show more detailed results.

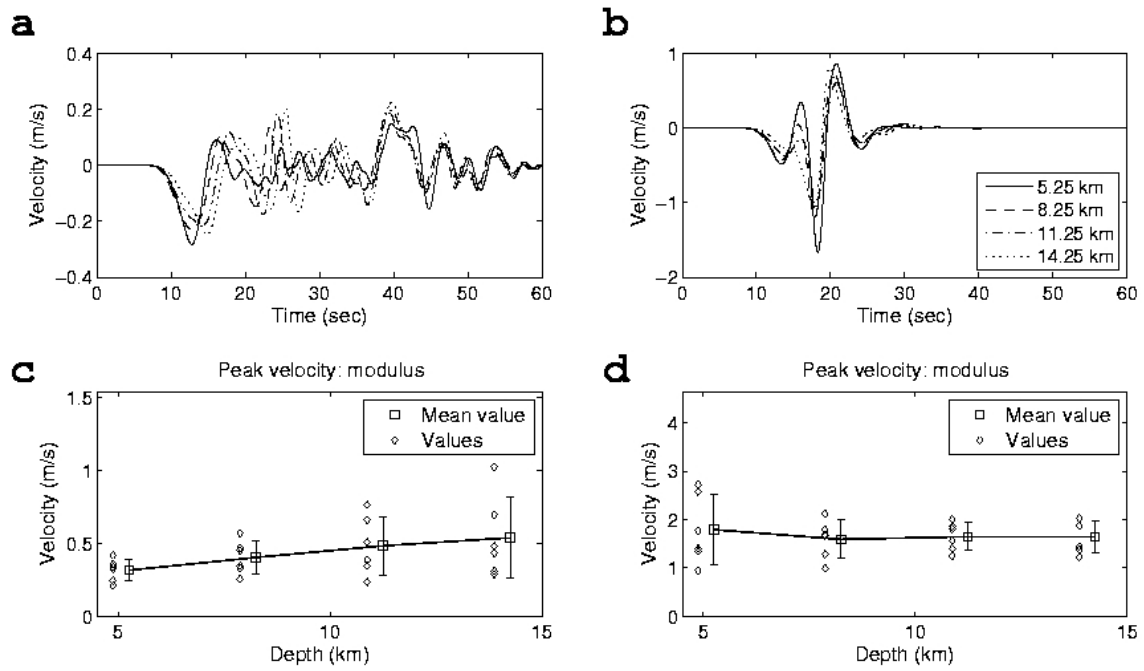


Figure 8: a+b: Velocity seismograms (fault-parallel component) for the M7 earthquake with same epicentre but varying source depth (see Fig. 3, inlet, white rectangle) at receivers indicated in Fig. 7c. **a.** R1, approx. 40 km off fault. **b.** R2, close to the fault trace. **c+d:** PGV as well as mean and variance for all simulations. **c.** R1; **d.** R2. Mean and variance are offset for illustrative reasons.